Long-range coupling regulates stator dynamics in the bacterial flagellar motor

Shabduli A. Sawant[1,2], I. Can Kazan[2,3], Brennen M. Wise[1,2,3], S. Banu Ozkan[2,3], and Navish Wadhwa[1,2,3]

[1]**Biodesign Center for Mechanisms of Evolution, Arizona State University, Tempe, AZ 85287, USA**

[2]**Center for Biological Physics, Arizona State University, Tempe, AZ 85287, USA**

[3]**Department of Physics, Arizona State University, Tempe, AZ 85287, USA**

Corresponding author:

Navish Wadhwa

Email address: navish.wadhwa@asu.edu

ABSTRACT

The bacterial flagellar motor is driven by stator complexes that couple ion flux to torque generation. Active stators dynamically exchange with a membrane pool in a load-dependent manner, with off-rates decreasing as motor load increases. Each stator comprises of MotA, which engages the rotor, and MotB, whose periplasmic domain anchors the complex to the peptidoglycan. But how external load regulates this anchoring remains unclear. Here, we show that long-range couplings within the *Escherichia coli* MotB periplasmic domain regulate stator dynamics. Computational modeling revealed that the flexible loops believed to anchor the stator to the peptidoglycan and P-ring are dynamically coupled to distant residues. Coevolutionary analysis reinforced these couplings, highlighting conserved communication pathways within the domain. Guided by these predictions, we introduced point mutations at key sites and assayed motility of cells harboring these mutations. Most mutants remained motile but displayed distinct swimming phenotypes. In agreement with computational predictions, measurements of swimming speed at different stator expression levels showed that several mutations altered stator dynamics. Finally, molecular dynamics simulations revealed that variation in dynamic flexibility of the loops strongly correlates with the observed swimming speeds *in vivo*. Together, these results demonstrate that flexibility and long-range coupling within MotB tune stator anchoring, providing new insight into mechanosensitive remodeling of the flagellar motor.

Keywords: bacterial flagellar motor; mechanosensing; dynamic coupling; co-evolution; molecular motor; protein dynamics

INTRODUCTION

Many bacteria use rotary flagella to navigate their environment, allowing them to swim towards resources and away from harm (Wadhwa and Berg, 2022). Beyond survival, motility is often essential for infection, surface attachment, and biofilm formation (Haiko and Westerlund-Wikström, 2013; Belas, 2014). The flagellum comprises a helical filament, a flexible hook, and a rotary motor embedded in the cell envelope (Nakamura and Minamino, 2024). The motor is powered by stator complexes, each made of MotA and MotB proteins in a 5:2 ratio (Stolz and Berg, 1991; Santiveri et al., 2020; Deme et al., 2020). The MotB dimer anchors the stator to the P-ring and the peptidoglycan cell wall (De Mot and Vanderleyden, 1994; Roujeinikova, 2008; Hizukuri et al., 2010), while the MotA pentamer rotates around it, exerting torque on the cytoplasmic rotor ring (Sowa and Berry, 2008) (Fig. 1A). Ion flow through the stator, driven by an electrochemical gradient across the inner membrane, powers this motion (Meister et al., 1987). The resulting flagellar rotation propels the cell through its viscous surroundings.

Despite their name, bacterial stators are often dynamic. In *Escherichia coli* and *Salmonella enterica*, stators continuously exchange between the motor and a membrane-embedded pool (Leake et al., 2006; Block and Berg, 1984; Blair and Berg, 1988). The *E. coli* motor can hold up to eleven stators (Reid et al., 2006), but typically operates with around five (Niu et al., 2023). Stator occupancy is load-dependent: fewer stators are engaged under low load, while high load recruits more to meet increased torque demand (Lele et al., 2013; Tipping et al., 2013; Nord et al., 2017; Wadhwa et al., 2019, 2021) (Fig. 1C). These dynamic changes allow the motor to adapt to varying physical environments (Wadhwa et al., 2022).

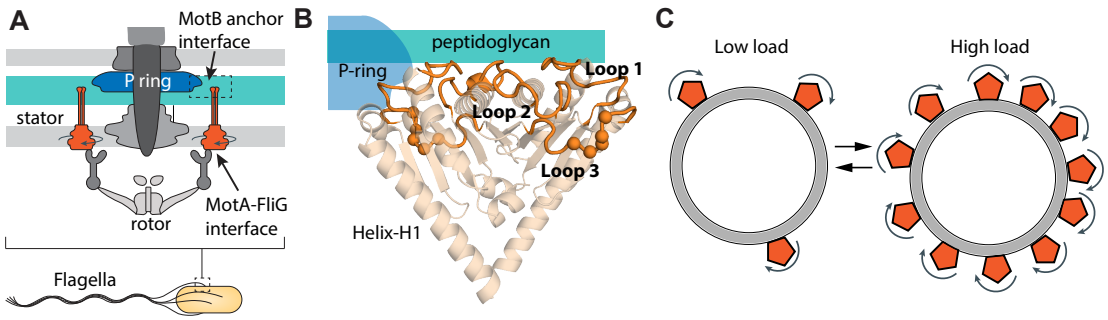

Figure 1. Load-dependent remodeling of torque-generating stators in the bacterial flagellar motor. **(A)** Structural components of the flagellar motor. Stator complexes (orange) generate torque in the motor. MotA interacts with the rotor (via FliG), while the periplasmic domain of MotB anchors the complex in the peptidoglycan near the P-ring (blue). **(B)** Structure of the *E. coli* MotB periplasmic domain, obtained from SWISS-MODEL. This domain anchors the stator to the peptidoglycan and P-ring. Peptidoglycan interfacing loops are highlighted and P-ring interacting residues are represented as spheres. **(C)** Load dependence of stator binding. At low load, stators exchange rapidly between the motor and the membrane pool. At high load, stator anchoring is stabilized, reducing their off-rate.

Previous work suggests that stator anchoring strengthens under high load (Nord et al., 2017; Wadhwa et al., 2019, 2021). As load increases, stators unbind from the motor less often, increasing the average dwell time (Nord et al., 2017; Wadhwa et al., 2021). This behavior resembles a catch-bond, one whose lifetime increases with mechanical stress (Prezhdo and Pereverzev, 2009). Load acts on the stator at the

MotA-rotor (FliG) interface, while anchoring occurs at the MotB periplasmic domain, which binds to the P-ring and peptidoglycan (Roujeinikova, 2008; Zhu et al., 2020) (Fig. 1B). Because these two interfaces are separated across the inner membrane and periplasm, load must be transmitted through the stator to modulate anchoring.

Conformational changes in MotB, including linker opening and dimerization of its periplasmic domain, regulate stator binding and activation by bridging the gap to the peptidoglycan layer (Kojima et al., 2009; Zhu et al., 2014; Kojima et al., 2018). In this active conformation, loops 1, 2 and 3 (Fig. 1B) from the periplasmic domain interact with the peptidoglycan and the flagellar P-ring (Hizukuri et al., 2010). Crystal structures of the *Helicobacter pylori* MotB periplasmic domain show that N-terminal linker truncations result in different conformations of the peptidoglycan-binding loops, suggesting that the linker affects loop dynamics despite their spatial separation (O'Neill et al., 2011). Together with their large conformational dynamics (Reboul et al., 2011), this suggests that the loops may act as dynamic clamps for peptidoglycan binding, with binding strength regulated remotely. Thus, we hypothesize that long-range allosteric interactions in the MotB periplasmic domain regulate stator remodeling in response to load by modulating anchoring with the peptidoglycan.

Here, we tested this hypothesis using Dynamic Flexibility Index (DFI) and Dynamic Coupling Index (DCI) analyses (Campitelli et al., 2020, 2025) on the *E. coli* MotB periplasmic domain. This revealed residues distally coupled to the peptidoglycan-interacting loops, many of which also showed signs of co-evolution (Kazan et al., 2022). Guided by these couplings, we introduced amino acid substitutions based on evolutionary sequence variability at these identified distal sites, and found that they modulated motility. By varying stator expression, we observed swimming trends distinct from wildtype, showing that several of the mutations affected stator dynamics. Molecular dynamics simulations revealed that variance in loop flexibilities of mutants correlates with the observed swimming speeds *in vivo*. Together, these results demonstrate that long-range, allosteric interactions help regulate stator dynamics and mechanical output in the bacterial flagellar motor, revealing a molecular mechanism by which bacteria tune their response to physical environments.

RESULTS

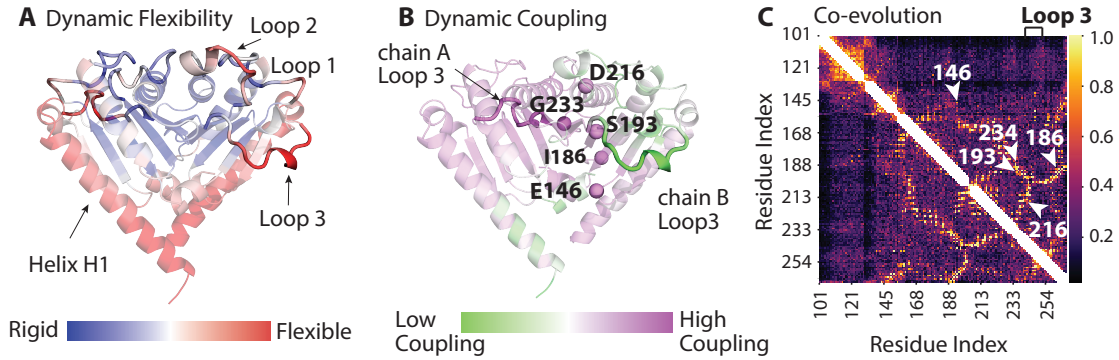

Figure 2. Dynamic and evolutionary couplings within the MotB periplasmic domain indicate conserved long-range interactions. (A) Flexibility profile of the MotB periplasmic domain. Flexible regions (red) and rigid regions (blue) are shown. Loops 2 and 3 at the peptidoglycan interface, along with helix H1, display higher flexibility. **(B)** Dynamic coupling of chain A loop 3 with other regions of the MotB periplasmic domain. High (violet) and low (green) coupling are shown. Residues in chain B that couple strongly with loop 3 in chain A are highlighted. **(C)** Evolutionary coupling heat map. Yellow indicates highly coupled residue pairs. Arrows mark residues that overlap with regions of high pctDCI in panel B, highlighting positions with both strong dynamic and evolutionary coupling.

Flexibility and long-range coupling in the MotB periplasmic domain

To investigate the dynamics of the *E. coli* MotB periplasmic domain, we generated its structural models using the homology modeling tool SWISS-MODEL (Waterhouse et al., 2018). We selected three models that corresponded to distinct conformational states observed in the X-ray structure of *Salmonella* MotB (Kojima et al., 2009) and were in agreement with predictions from AlphaFold3 (Fig. S1). Transmission of mechanical information requires both flexible and rigid sites, prompting us to determine the dynamic profile of this domain using the Dynamic Flexibility Index (DFI) (see Materials and Methods). Low DFI values indicate rigidity while high values indicate flexibility (Gerek et al., 2013). Across all three models, the P-ring-interfacing loop 3 and the H1 helix consistently showed high flexibility, along with portions of loop 2 (Fig. 2A and Fig. S2). These dynamic signatures align with previous observations in the *H. pylori* MotB periplasmic domain (Reboul et al., 2011). Based on this, we speculated that the flexibility of loops 2 and 3 may allow them to act as dynamic clamps, modulating interactions at the MotB–peptidoglycan interface.

For regulating stator anchoring, load information must be transmitted from distal mechanically coupled sites to the peptidoglycan interface. To identify these, we performed Dynamic Coupling Index (DCI) analysis (Ose et al., 2022) which quantifies how strongly any given residue is coupled to a defined active site. Given loop 3's high flexibility in DFI and its known interaction with the P-ring (Hizukuri et al., 2010), we designated it as the active site. As expected, many residues within the same chain showed strong coupling to loop 3, reflecting tight intra-chain interactions (Fig. 2B). Notably, we also identified high DCI values in regions of the other chain of the dimer subunit. Specifically, residues 148–149, 180–194, 210–220, and 232–242 in chain B were strongly coupled to loop 3 from chain A. While residues 210–220 and

232–242 lie at the dimer interface, some residues from 148–149 and 180–194 are located at the opposite end of the MotB periplasmic domain, farthest from loop 3, making direct interactions unlikely. These intra- and inter-chain couplings indicate that MotB harbors structurally encoded pathways for modulating dynamics at distal sites within the periplasmic domain.

Coevolution supports long-range functional coupling in MotB periplasmic domain

Coevolution of residues within a protein often reflects functionally important interactions (Kowarsch et al., 2010; Butler et al., 2018). We therefore analyzed the MotB sequence for co-evolving residue pairs linking the peptidoglycan interface to distant sites within its periplasmic domain. For this we used EVcouplings, which derives this information from multiple sequence alignments (Hopf et al., 2019). While strong coevolution is typically observed between spatially proximal residues, coevolution between residues separated by more than $\sim$7 Å threshold for direct C-α contacts (Yuan et al., 2012) indicates long-range functional coupling. Indeed, we identified residues with both high evolutionary coupling probability and high DCI across distant parts of the periplasmic domain (Fig. 2C). For example, I186 showed strong evolutionary coupling with I260 despite being separated by 21 Å within a monomer and 30 Å across the dimer. E146 and S193 likewise showed high evolutionary coupling, with intra-chain and inter-chain distances of 14 Å and 20 Å, respectively. D216 at the dimer interface showed strong coevolution with several loop 2 residues (206–209), with intra- and inter-chain separations of $\sim$12 Å. The finding that residues dynamically coupled to loop 3 also coevolve with distal sites supports a functional role for these couplings. Table S1 shows a summary of the DCI, DFI, and co-evolution analysis.

Targeted mutations reveal regulatory roles of key MotB residues

From DFI and DCI analyses, we identified candidate sites for testing effect on stator functionality through point mutations. Within regions structurally coupled with loop 3, we selected residues that exhibited long-range coevolution and covered a broad range of dynamic flexibility. This yielded six positions: two flexible (E146, I186), two rigid (S193, D216), and one intermediate (G233). As a control, we also included a site within loop 3 (L247). To select positions that would not abolish function, we used amino acid conservation probabilities from ConSurf (Fig. S3). We also introduced charge-altering mutations at selected sites to test the effects of more dramatic substitutions. We expressed the mutant stators under an arabinose-inducible promoter (pBAD33) in *E. coli* MG1655 cells deleted for WT stators.

All mutations except one active site mutant, L247P, were functional, i.e., cells with these mutant stators were motile (Fig. 3A), albeit to different degrees in both liquid and soft agar supplemented with 0.02% arabinose for induction. With similar growth rates across strains (Fig. S4), variations in motility halos can be attributed to MotB mutations. Motility trends of single cells in buffer matched halo sizes in swim agar (Fig. 3B,C), confirming that the differences in halos arose from mutation-driven changes in swimming. Mutations I186V, S193T, and the active-site mutant L247A reduced swimming speed. In contrast, the D216N mutation caused an increase in swimming speed. Other substitutions (I186Q, I186L,

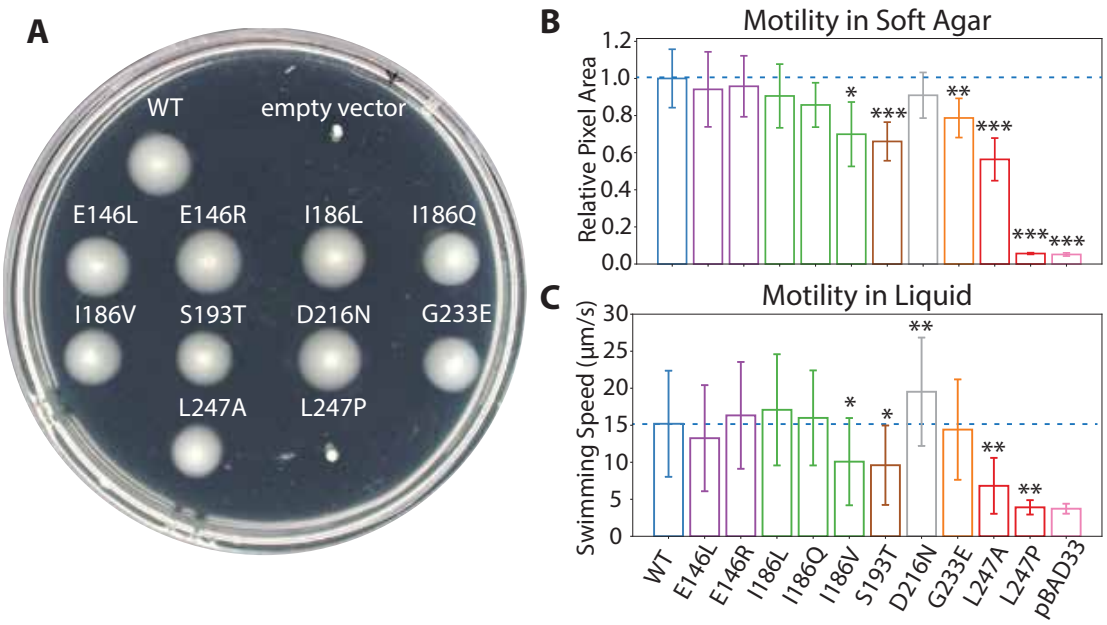

Figure 3. Cells expressing MotB stator mutants exhibit similar motility trends in semi-solid and liquid media. (A) Swimming motility in soft agar. Representative phenotypes of *motB* stator mutants expressed from the pBAD33 plasmid in 0.25% soft agar with 0.02% arabinose induction. **(B)** Quantification of motility halo size. Halo areas normalized to WT *motAB* expressed from pBAD33 at the same induction level. Error bars indicate standard deviation. Sample size $n = 8$ per mutant. $*$ represents $p < 0.05$, $**$ represents $p < 0.01$, and $***$ represents $p < 0.001$ from a Student's t-test against the WT values. **(C)** Swimming motility in liquid. Mean swimming speeds of *E. coli* cells in motility buffer expressing motB mutants. Error bars indicate standard deviation. p-values are obtained from a Welch's t-test against the WT values. A t-test was not conducted for the empty vector.

E146L, E146R, G233E) yielded speeds comparable to WT. In general, cells expressing mutant MotB stators remained motile, with some mutants exhibiting distinct swimming speed trends compared to wild type (Fig. 3C). Thus, mutations at dynamically coupled sites within the periplasmic domain influence swimming motility *in vivo*.

Long-range interactions tune motility by modulating stator dynamics

Differences in swimming speed can reflect a difference in torque production but can also arise from a change in the number of active stators. To investigate this, we varied mutant stator expression over a wide range of inducer concentrations (2×10^{-5}%–2% Arabinose w/v) and quantified swimming speeds by tracking individual cells swimming in liquid (Fig. S5). Increasing the cellular stator pool increased the number of motor-bound stators, as reflected by higher swimming speeds with arabinose in all mutants except the non-motile L247P (Fig. 4A). However, because the motor can accommodate only a limited number of stators (Reid et al., 2006), occupancy and swimming speed should saturate at high expression, and residual differences are due to torque differences. Conversely, if mutants converge at saturation, speed differences at intermediate expression indicate differences in stator binding.

Except for three mutants (I186V, S193T, and L247A) and the non-motile mutant (L247P), all other mutants saturated at wild type levels of swimming speed, suggesting similar torque production as wild type (Fig. 4A). However, differences in their swimming speeds at intermediate expression levels indicated

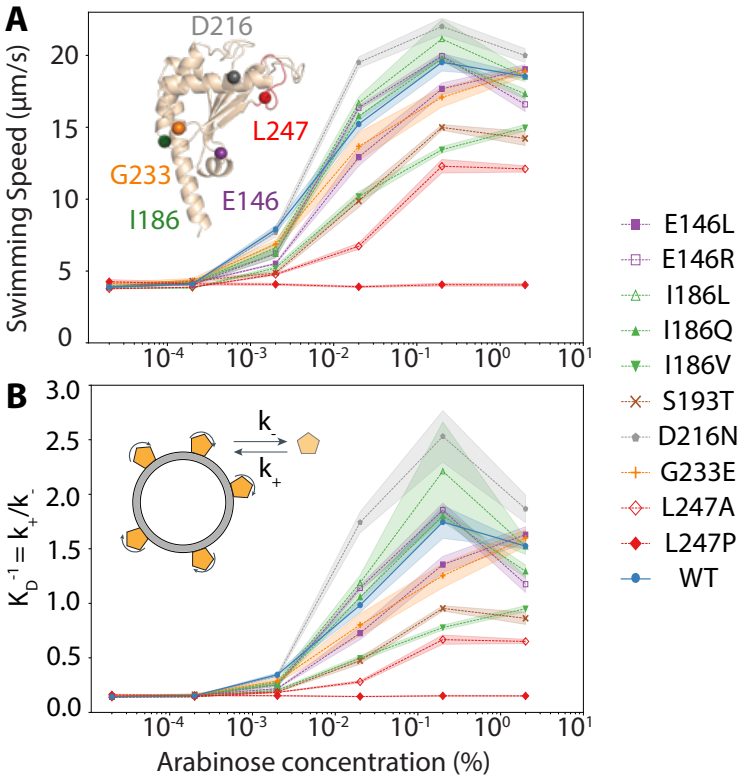

Figure 4. Expression-dependent motility and stator kinetics. (A) Swimming speed as a function of arabinose concentration. Mean speeds of *E. coli* cells expressing WT or mutant *motB* from pBAD33 at induction levels ranging from 2×10^{-5}% to 2% arabinose. Shaded regions indicate standard error of the mean. **(B)** Stator binding and unbinding kinetics. Ratio of association and dissociation rates (K_D^{-1}) for WT and mutant stators across the same induction series. Shaded regions indicate standard error of the mean.

differences in stator dynamics. D216N swam faster than WT at intermediate expression levels, most notably at 0.02% arabinose, whereas I186L produced only a modest increase at one expression level. Two mutants (E146L and G233E) swam slower than WT at intermediate expression levels, yet reached WT-like saturation speeds. E146R and I186Q showed swimming trends similar to WT at all expression levels.

Assuming each stator within a motor contributes equally to torque, swimming speed can serve as a readout of the number of bound stators. Using MG1655 cells (Fig. S6), which typically operate with about five stators per motor (Niu et al., 2023), we calibrated swimming speed to stator occupancy and obtained a conversion factor of 2.8 μm/s/stator. This calibration allowed us to estimate stator occupancy for each mutant directly from swimming speeds (Fig. S7). Stator occupancy increased with expression and saturated at high levels, consistent with the stator reaching close to full capacity. Using the Hill-Langmuir model (Nord et al., 2017; Wadhwa et al., 2019) for stator assembly, we extracted the dissociation constant $K_D = k_-/k_+$ across arabinose concentrations. We describe our results in terms of $K_D^{-1} = k_+/k_-$ for ease of interpretation (Fig. 4B).

Differences in K_D^{-1} across mutants can reflect changes in k_+, k_-, or both, but in all cases indicate altered stator anchoring through long-range regulation of interaction interfaces by distal mutations. D216N and I186L showed higher K_D^{-1} at intermediate expression, consistent with their faster swimming than WT. L247P showed a K_D^{-1} close to 0, consistent with this mutant being nonmotile. E146L and G233E had lower K_D^{-1} yet reached full capacity at higher expression, indicating weaker stator anchoring. S193T, I186V, and L247A showed both reduced K_D^{-1} and saturation below WT, suggesting that one or both of the rates were significantly altered. These analyses confirm that key residues in MotB's periplasmic domain, outside the interfacial loops, tune stator binding kinetics, with substantial consequences for cell motility.

Loop flexibility of mutant stators predicts their anchoring dynamics

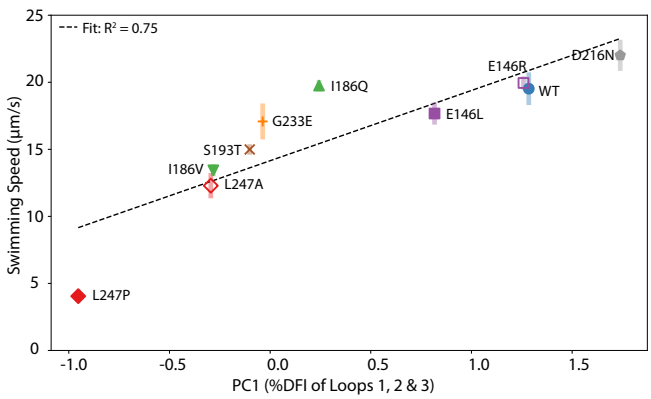

Figure 5. Correlation between loop dynamics and mean swimming speeds at 0.2% arabinose of MotB variants. Principal component analysis (PCA) was applied to the dynamic flexibility index (DFI) profiles of the peptidoglycan-binding loops. The first principal component (PC1) strongly correlates with motility-derived binding affinities (R = 0.866, p = 1.21×10^{-3}). Each point represents a MotB variant and the shaded region represents the standard error, with the nonfunctional loop mutant L247P and the fast swimming distal mutant D216N lying at opposite extremes, highlighting that both local and distal substitutions can dampen or amplify loop flexibility to tune stator function.

To probe how these mutations influence the dynamics of the peptidoglycan-binding loops, we computed dynamic flexibility index (DFI) profiles for each MotB variant using molecular dynamics simulations. DFI quantifies the relative flexibility of each residue in the context of the global protein network dynamics (see Materials and Methods), thereby capturing how local loop motions are dynamically dampened or amplified by mutation. Indeed, the DFI profile of each variant shows changes compared to wild type (Fig. S8). We then applied principal component analysis (PCA), a dimensionality reduction method that extracts the dominant sources of variation across the DFI profiles of loop regions interacting with the peptidoglycan. Strikingly, the first principal component (PC1), which captures the largest variance in loop dynamics, showed a strong correlation with the experimentally measured swimming speeds ($R = 0.866$, $p = 1.21 \times 10^{-3}$) (Fig. 5). Thus, mutation-driven alterations in loop dynamics directly underlie changes in stator function. Particularly, the nonfunctional mutant L247P, which abolishes motility, and the D216N mutant, which yields the faster swimming phenotype, occupy the two extremes of the PCA axis. Importantly, while L247P resides within the loop itself, D216N lies outside the binding loop, demonstrating that long-range allosteric modulation can rewire loop flexibility to tune function. These findings highlight that both local perturbations and distal allosteric substitutions can reshape loop dynamics, thereby governing MotB's ability to engage the cell wall and power motility.

DISCUSSION

The bacterial flagellar motor adapts to changing external conditions through mechanosensitive remodeling of its stators. Here, we show that this process is regulated by dynamic and long-range couplings within the MotB periplasmic domain. Our combined computational and experimental analyses demonstrate that variations in flexibility in this domain tunes stator binding and torque output, providing a mechanistic link between structure, dynamics, and function.

Dynamic flexibility and coupling analyses identified loops 2 and 3 as flexible elements coupled to distant residues across the MotB dimer, suggesting long-range allosteric regulation of stator anchoring. As expected, coevolution captured patterns similar to the dynamic coupling index, assigning higher values to the residues in close proximity in the 3D folded structure of the protein and lower values to those distant from each other. However, both these methods independently highlighted strong coupling probabilities for residue pairs that were spatially well-separated within the monomer as well as the dimer structure of the domain. This suggested that these interactions are functionally important and conserved across species. Together, these analyses highlight a structurally-encoded network within the MotB periplasmic domain for transmitting mechanical information.

Targeted mutagenesis, guided by these predictions, revealed distinct motility phenotypes, where some mutants showed significantly faster or slower speeds compared to wild type (Fig. 3B,C). Arabinose-titration results showed speeds of some mutants diverging from wildtype at intermediate stator expression but eventually saturating at the same speed as wildtype (Fig. 4A). These experiments distinguished mutations

that altered stator binding rates from those that potentially reduced torque per stator. Importantly, residues far from the binding interface influenced stator dynamics *in vivo*, consistent with regulation through long-range coupling.

Our model indicates, given specific assumptions, that the kinetic rates of stators are changed by these mutations (Fig. 4B). The calculation of K_D^{-1} assumes that each mutant stator produces the same torque (see Materials and Methods). If this assumption was broken, we would expect to see behavior like that of the S193T, I186V, and L247A mutants. A possible explanation is that these three mutant stators have lower torque than WT, resulting in an increased k_- value. If this is the case, the reported K_D^{-1} values for these three mutants are overestimates of the true value. Thus, mutations outside loop 3 can alter either binding or torque. This is not entirely surprising, since we know from previous work that stator anchoring and torque output are closely coupled through mechanosensitive remodeling (Tipping et al., 2013; Nord et al., 2017; Wadhwa et al., 2019, 2021, 2022).

Although the stator interacts with the rotor via MotA, the load information must reach the MotB-peptidoglycan interface to enable the observed mechanosensitive response of stators (Nord et al., 2017). Our work shows that interactions at this interface can be tuned by residues located outside it, providing a plausible mechanism for mechanosensitive control. Load acting on an active stator adds resistance to MotA's rotation around MotB. This stress at the MotA-FliG interface must propagate through the proton channel (the site of torque generation in MotA-MotB interface) and towards the peptidoglycan anchoring site of MotB (Che et al., 2008), through the open plug-linker and periplasmic domain. We speculate that the residues identified in this study lie on the path of stress transmission, and that their dynamic coupling with flexible loops regulates stator anchoring in a load-dependent manner. The strong correlation of swimming speed of these mutants with loop dynamics lends support to this model of long-range regulation of a load-dependent catch-bond.

More broadly, long-range coupling is a common feature of allosteric proteins (Monod et al., 1965; Süel et al., 2003; Reynolds et al., 2011), and our results suggest that bacterial stators exploit this principle to enable stable anchoring while simultaneously permitting dynamic regulation. Future work combining structural studies with direct single-molecule measurements will help refine this model and fully map the pathways that regulate stator function.

MATERIALS AND METHODS

Modeling MotB periplasmic domain

We modeled the *E. coli* MotB periplasmic domain using SWISS-MODEL and selected three of the top ten predictions (models 01, 05 and 07), each corresponding to a disctinct crystal form. We compared these models with structural prediction of the MotB periplasmic domain from AlphaFold by superimposing them in PyMOL. The overall root mean squared deviation (RMSD) values between the AlphaFold prediction and model 01, model 05 and model 07 were 0.702, 0.749 and 0.732 respectively.

Dynamic flexibility index (DFI)

The dynamic flexibility index (DFI) is a residue-specific metric that quantifies how resistant a protein position is to force perturbations. It measures the relative fluctuation response of a residue compared to the overall fluctuation response of the protein (Kumar et al., 2015; Larrimore et al., 2017). The method is based on linear response theory applied within either molecular dynamics (MD)–derived covariance matrices or coarse-grained elastic network models (ENMs).

To compute DFI, we perturb each residue sequentially with a small, random Brownian force and calculate the fluctuation response of all residues. The displacement response vector ΔR is obtained from the linear response relationship:

$$[\Delta R]_{3N\times 1} = [H^{-1}_{3N\times 3N}][F]_{3N\times 1} \tag{1}$$

where F is the perturbing force vector, and H is the Hessian matrix of second derivatives of the potential energy. The inverse Hessian, H^{-1}, corresponds to the covariance matrix that captures residue–residue couplings. Forces are applied in multiple directions to approximate isotropic fluctuations, and the averaged responses are used to obtain residue-level profiles.

The DFI of residue i is then defined as:

$$\mathrm{DFI}i = \frac{\sum_{j=1}^{N} |\Delta R^j|i}{N \sum_{i=1}^{N} |\Delta R^j|_i} \tag{2}$$

Here, $|\Delta R^j|_i$ is the magnitude of the displacement of residue i in response to perturbation at residue j, and the denominator normalizes by the total response across the protein. Thus, the DFI represents the fractional contribution of residue i to the global fluctuation response.

Residues with low DFI values (<0.2) act as hinge points within the interaction network. These sites typically exhibit limited local fluctuations yet serve as effective conduits for transmitting perturbations, thereby exerting control over collective motions. In contrast, high-DFI residues are dynamically more flexible and

less constrained by network interactions. Prior studies have shown that mutations at low-DFI positions often disrupt communication pathways and lead to functional changes or disease associations (Campitelli et al., 2020, 2025). Substitutions at such sites frequently modify catalytic activity, ligand binding, or allosteric communication by shifting equilibrium dynamics.

In this study, covariance matrices used for DFI calculations were obtained from both MD simulations (for all variant and WT) and ENM (Fig. 2). The resulting DFI profiles were then analyzed using principal component analysis (PCA) to identify dominant dynamical trends associated with MotB function.

Dynamic Coupling Index (DCI)

The dynamic coupling index (DCI) quantifies how strongly the fluctuation response of residue i is coupled to perturbations at a specific residue j, relative to its average response to perturbations at all residues in the protein. Thus, DCI compares a specific response to a global baseline response, highlighting preferential dynamic couplings between residues.

Formally, the DCI of residue i with respect to residue j is defined as:

$$\mathrm{DCI}_i^j = \frac{|\Delta\vec{R}^j|i}{\frac{1}{N}\sum_{k=1}^{N}|\Delta\vec{R}^k|_i} \tag{3}$$

Here, $|\Delta\vec{R}^j|i$ is the fluctuation response of residue i to perturbation at residue j, and the denominator represents the average fluctuation response of residue i to perturbations across all N residues. A value of $\mathrm{DCI}_i^j > 1$ indicates that residue i is more strongly coupled to j than expected on average, whereas $\mathrm{DCI}_i^j < 1$ indicates weaker-than-average coupling.

DCI has been widely used to identify residues that mediate long-range communication, even when separated by large structural distances. For example, residues far from the active site can exhibit high DCI with catalytic residues, implicating their role in allosteric regulation (Campitelli and Ozkan, 2019; Campitelli et al., 2020). Beyond enzymes, DCI has been applied to uncover the role of distal sites in viral protein allostery, protein–RNA interactions, and viral capsid assembly (Hamilton et al., 2024; Ose et al., 2024).

Together with DFI, which identifies flexible and rigid communication hubs, DCI provides a complementary measure of residue–residue coupling that enables the detection of allosteric pathways and mechanistic insights into how mutations reshape protein dynamics.

Co-evolution

The method to compute co-evolution relies on sequence information to build a matrix of structural contacts. We used the EVcouplings (Hopf et al., 2019) server to gather information on evolutionary couplings (ECs) within the MotB periplasmic domain. While these analyses are generally used to predict protein 3D structures as residue pairs with high ECs are expected to be in close proximity (Hopf et al., 2014),

using our model structures we identified structurally distant residue pairs showing high evolutionary coupling. From the 12967 co-evolving pairs in the entire MotB sequence, we selected 328 pairs having a co-evolution probability equal to and above 80%. Because residue co-evolution is also an indicator of direct interactions in the folded protein (Hopf et al., 2012), we calculated distances between the C-α atoms of the co-evolving residue pairs in the folded structure of the MotB periplasmic domain to identify residue pairs that were spatially separated across different regions of the protein. Distant co-evolving residue pairs which also showed a high DCI value were found to be divided into three categories by further integrating information from the DFI analysis —1) flexible and co-evolutionarily coupled (E146 and I186), rigid and 2) co-evolutionarily coupled (S193 and D216) and 3) intermediate flexibility and co-evolutionarily coupled (G234).

Bacterial Strains, Plasmids, and Cultures

All strains used here were derivatives of the *E. coli* strain MG1655. Strain NW165 was deleted for *motAB* using the lambda red scar-less recombination method (Murphy and Campellone, 2003) with a modified counter-selection system (Kim et al., 2020). To investigate the motility phenotype of mutant stators, plasmids expressing these mutants were constructed by first cloning *motAB* in pBAD33 using the NEBuilder HiFi DNA Assembly cloning kit. The pBAD33-*motAB* plasmid was then used as a template for the site-directed mutagenesis of MotB using Agilent's Quick Change Kit. The resulting plasmids expressing *motA* along with one of the *motB* variants were then transformed into NW165.

Cells were grown by diluting an overnight culture 1:100 in TB (10 g/L tryptone, 5 g/L NaCl) supplemented with 25 µg/mL chloramphenicol, followed by incubation at 37°C with shaking at 200 rpm to $OD_{600} = 0.3$. Cells were then induced with $2 \times 10^{-5} - 2\%$ arabinose until OD_{600} reached a range of 0.4–0.6.

Soft agar assay

TB soft agar was prepared by dissolving 10 g/L tryptone, 5 g/L NaCl and 2.5 g/L of Difco agar in Milli-Q water and autoclaved. 25 mL of soft agar was poured into standard petri plates and supplemented with filter-sterilized arabinose at a final concentration of 0.02% . A well isolated bacterial colony was picked with a 20 μL pipette tip and stabbed till halfway in the solidified soft agar. Plates were incubated at 30°C for 14-15 h. Plates were imaged using custom-built imaging setup, and motility halo sizes were measured using an in-house written script in Python.

Swimming speed measurements

Cells were harvested by centrifugation at 1500 g for 7 min. The pellet was re-suspended in a motility buffer (10 mM potassium phosphate, 0.1 mM EDTA, 10 mM lactic acid, 1mM methionine and 66.7 mM NaCl, pH 7.4). The cell suspension was diluted 50X ($OD_{600}\sim0.01$), introduced into a 65 µL geneframe (Thermo Fisher Scientific), and sealed with a glass cover slip. 1 minute long recordings of freely swimming

cells were made using a 20X objective at 20 frames per second using ThorLabs (model DCC1545M) camera. Cell tracking and speed measurements of individual cells were performed using Trackmate in ImageJ (Tinevez et al., 2017; Schindelin et al., 2012). Average swimming speeds were calculated using TrackMate's SimpleSparseLAPTracker algorithm (Jaqaman et al., 2008) which is suitable for particles undergoing Brownian motion. We only used tracks longer than 15 frames to avoid noise from spurious tracks. Finally, we converted the pixel/frame speed values from TrackMate to μm/s by multiplying with a conversion factor obtained with a stage micrometer.

Estimating stator occupancy and K_D^{-1} from swimming speeds

All stators in a motor generate the same torque (Block and Berg, 1984), and thus contribute equally to rotation frequency. Assuming the number of motors per cell is constant across mutants, the mean swimming speed can be expressed as

$$\langle v_{\text{swim}} \rangle = \beta \langle N_{\text{ss}} \rangle, \tag{4}$$

where $\langle v_{\text{swim}} \rangle$ is the population-averaged swimming speed, $\langle N_{\text{ss}} \rangle$ is the mean steady-state number of bound stators per motor, and β is a proportionality constant. β was taken to be constant across mutants because factors that determine it (e.g., number of flagella per cell, hydrodynamic thrust per flagellum) should not be affected by point mutations in stators.

WT *E. coli* cells typically swim with $\langle N_{\text{ss}} \rangle \approx 5$ stators in standard motility buffer (Niu et al., 2023). From this and our measured WT swimming speed, we estimated $\beta = 2.8$ μm/s/stator. With this calibration, $\langle N_{\text{ss}} \rangle$ was calculated for each mutant (S7).

If stator binding and unbinding rates are k_+ and k_-, respectively, the steady-state occupancy follows a Hill-Langmuir model (Nord et al., 2017; Nirody et al., 2019):

$$\langle N_{\text{ss}} \rangle = \frac{N_{\text{max}}}{1 + \frac{k_-}{k_+}} = \frac{N_{\text{ss}}}{1 + K_D}, \tag{5}$$

where $N_{\text{max}} = 11$ is the maximum number of stators per motor (Reid et al., 2006). From this formulation, we estimated K_D^{-1} for each mutant and for all arabinose concentrations tested.

Molecular Dynamics Simulations

Molecular dynamics (MD) simulations were performed using the AMBER 20 software package to investigate the dynamic properties of wild-type MotB and selected mutants. The starting structural model was obtained from a previously described SWISS-MODEL homology model. Point mutations were introduced in PyMOL, and the ff14SB force field was used for protein parameterization. Each system was solvated in a rectangular box of TIP3P water molecules, ensuring a minimum distance of 16 Å between any protein atom and the box boundaries. Charge neutrality was achieved by adding Na^+ and Cl^- counterions.

The simulation protocol consisted of three main stages: energy minimization, equilibration, and

production. Energy minimization was carried out in two steps. First, 100,000 cycles of steepest descent minimization were applied with positional restraints on protein and solvent heavy atoms, allowing relaxation of the water molecules. This was followed by unrestrained minimization, during which the SHAKE algorithm was applied to constrain covalent bonds involving hydrogens. After minimization, the system was gradually heated from 0 K to 300 K over 50,000 steps with a 2 fs timestep, using harmonic restraints on protein heavy atoms. Hydrogen atom constraints were maintained throughout the heating stage. Equilibration was then performed under constant pres-sure and temperature (NPT) conditions to stabilize both system density and pressure.

Production simulations were conducted under NPT ensemble conditions at 300 K and 1 bar. Temperature was regulated using a Langevin thermostat with a collision frequency of 1.0 ps^{-1}, and pressure was controlled using a Berendsen barostat. A timestep of 2 fs was used, with SHAKE applied to constrain bonds involving hydrogens. Each system, including the wild type and all selected mutants, was simulated for 2 μs of production dynamics, providing sufficiently long trajectories for comparative analysis of slow conformational changes. To ensure adequate sampling, trajectory convergence was carefully evaluated following established methods (Kazan et al., 2023).

Finally, we applied principal component analysis (PCA) to DFI from MD simulations to segregate the MotB mutants by dynamics. This approach enables dimensionality-reduction by a linear combination of original variables into principal components (PCs) which capture the largest variability from the data (Jolliffe, 2005).

AUTHOR CONTRIBUTIONS

S.A.S., S.B.O., and N.W. designed the research; N.W. and S.B.O. oversaw the research; S.A.S. performed experiments; S.A.S., B.M.W. and I.C.K. analyzed data; I.C.K. performed MD simulations; S.A.S., S.B.O., and N.W. wrote the manuscript.

FUNDING

This work is supported by the National Institute of General Medical Sciences of the National Institutes of Health (Grant R01GM147635 to S.B.O and Grant R00GM134124 to N.W), Gordon and Betty Moore Foundation (AWD0003443 to S.B.O), and the Arizona Biomedical Research Centre (Award RFGA2023-008-14 to N.W).

ACKNOWLEDGMENTS

We thank Karen Fahrner and Carolina Gogerty for helpful suggestions on strain construction, Keichi Namba and Mayra Garcia-Alcala for sharing plasmids, and Ngoc Huynh and Nikhil Ramesh for sharing data visualization scripts. We are also grateful to all members of the Wadhwa lab for their insightful discussions and feedback throughout this study.

CONFLICTS OF INTEREST

The authors declare no conflict of interest.

REFERENCES

Belas, R. (2014). Biofilms, flagella, and mechanosensing of surfaces by bacteria. *Trends in Microbiology*, 22(9):517–527.

Blair, D. F. and Berg, H. C. (1988). Restoration of torque in defective flagellar motors. *Science*, 242(4886):1678–1681.

Block, S. M. and Berg, H. C. (1984). Successive incorporation of force-generating units in the bacterial rotary motor. *Nature*, 309(5967):470–472.

Butler, B. M., Kazan, I. C., Kumar, A., and Ozkan, S. B. (2018). Coevolving residues inform protein dynamics profiles and disease susceptibility of nsnvs. *PLoS Computational Biology*, 14(11):e1006626.

Campitelli, P., Kazan, I. C., Hamilton, S., and Ozkan, S. B. (2025). Dynamic allostery: Evolution's double-edged sword in protein function and disease. *Journal of Molecular Biology*, page 169175.

Campitelli, P., Modi, T., Kumar, S., and Ozkan, S. B. (2020). The role of conformational dynamics and allostery in modulating protein evolution. *Annual Review of Biophysics*, 49(1):267–288.

Campitelli, P. and Ozkan, S. B. (2019). *Allostery and Structural Dynamics in Protein Evolution*, pages 179–194. Springer International Publishing, Cham.

Che, Y.-S., Nakamura, S., Kojima, S., Kami-ike, N., Namba, K., and Minamino, T. (2008). Suppressor analysis of the motb (d33e) mutation to probe bacterial flagellar motor dynamics coupled with proton translocation. *Journal of Bacteriology*, 190(20):6660–6667.

De Mot, R. and Vanderleyden, J. (1994). The c-terminal sequence conservation between ompa-related outer membrane proteins and motb suggests a common function in both gram-positive and gram-negative bacteria, possibly in the interaction of these domains with peptidoglycan. *Molecular Microbiology*, 12(2):333–334.

Deme, J. C., Johnson, S., Vickery, O., Aron, A., Monkhouse, H., Griffiths, T., James, R. H., Berks, B. C., Coulton, J. W., Stansfeld, P. J., et al. (2020). Structures of the stator complex that drives rotation of the bacterial flagellum. *Nature Microbiology*, 5(12):1553–1564.

Gerek, Z. N., Kumar, S., and Ozkan, S. B. (2013). Structural dynamics flexibility informs function and evolution at a proteome scale. *Biophysical Journal*, 104(2):228a.

Haiko, J. and Westerlund-Wikström, B. (2013). The role of the bacterial flagellum in adhesion and virulence. *Biology*, 2(4):1242–1267.

Hamilton, S., Modi, T., Šulc, P., and Ozkan, S. B. (2024). Rna-induced allosteric coupling drives viral capsid assembly. *PRX Life*, 2:013012.

Hizukuri, Y., Kojima, S., and Homma, M. (2010). Disulphide cross-linking between the stator and the bearing components in the bacterial flagellar motor. *The Journal of Biochemistry*, 148(3):309–318.

Hopf, T. A., Colwell, L. J., Sheridan, R., Rost, B., Sander, C., and Marks, D. S. (2012). Three-dimensional structures of membrane proteins from genomic sequencing. *Cell*, 149(7):1607–1621.

Hopf, T. A., Green, A. G., Schubert, B., Mersmann, S., Schärfe, C. P., Ingraham, J. B., Toth-Petroczy, A., Brock, K., Riesselman, A. J., Palmedo, P., et al. (2019). The evcouplings python framework for coevolutionary sequence analysis. *Bioinformatics*, 35(9):1582–1584.

Hopf, T. A., Schärfe, C. P., Rodrigues, J. P., Green, A. G., Kohlbacher, O., Sander, C., Bonvin, A. M., and Marks, D. S. (2014). Sequence co-evolution gives 3d contacts and structures of protein complexes. *eLife*, 3:e03430.

Jaqaman, K., Loerke, D., Mettlen, M., Kuwata, H., Grinstein, S., Schmid, S. L., and Danuser, G. (2008). Robust single-particle tracking in live-cell time-lapse sequences. *Nature Methods*, 5(8):695–702.

Jolliffe, I. (2005). Principal component analysis. *Encyclopedia of Statistics in Behavioral Science*.

Kazan, I. C., Mills, J. H., and Ozkan, S. B. (2023). Allosteric regulatory control in dihydrofolate reductase is revealed by dynamic asymmetry. *Protein Science*, 32(8):e4700.

Kazan, I. C., Sharma, P., Rahman, M. I., Bobkov, A., Fromme, R., Ghirlanda, G., and Ozkan, S. B. (2022). Design of novel cyanovirin-n variants by modulation of binding dynamics through distal mutations. *Elife*, 11:e67474.

Kim, J. M., Garcia-Alcala, M., Balleza, E., and Cluzel, P. (2020). Stochastic transcriptional pulses orchestrate flagellar biosynthesis in escherichia coli. *Science Advances*, 6(6):eaax0947.

Kojima, S., Imada, K., Sakuma, M., Sudo, Y., Kojima, C., Minamino, T., Homma, M., and Namba, K. (2009). Stator assembly and activation mechanism of the flagellar motor by the periplasmic region of motb. *Molecular Microbiology*, 73(4):710–718.

Kojima, S., Takao, M., Almira, G., Kawahara, I., Sakuma, M., Homma, M., Kojima, C., and Imada, K. (2018). The helix rearrangement in the periplasmic domain of the flagellar stator b subunit activates peptidoglycan binding and ion influx. *Structure*, 26(4):590–598.

Kowarsch, A., Fuchs, A., Frishman, D., and Pagel, P. (2010). Correlated mutations: a hallmark of phenotypic amino acid substitutions. *PLoS Computational Biology*, 6(9):e1000923.

Kumar, A., Glembo, T. J., and Ozkan, S. B. (2015). The role of conformational dynamics and allostery in the disease development of human ferritin. *Biophysical Journal*, 109(6):1273–1281.

Larrimore, K. E., Kazan, I. C., Kannan, L., Kendle, R. P., Jamal, T., Barcus, M., Bolia, A., Brimijoin, S., Zhan, C.-G., Ozkan, S. B., et al. (2017). Plant-expressed cocaine hydrolase variants of butyrylcholinesterase exhibit altered allosteric effects of cholinesterase activity and increased inhibitor sensitivity. *Scientific Reports*, 7(1):10419.

Leake, M. C., Chandler, J. H., Wadhams, G. H., Bai, F., Berry, R. M., and Armitage, J. P. (2006). Stoichiometry and turnover in single, functioning membrane protein complexes. *Nature*, 443(7109):355–358.

Lele, P. P., Hosu, B. G., and Berg, H. C. (2013). Dynamics of mechanosensing in the bacterial flagellar motor. *Proceedings of the National Academy of Sciences*, 110(29):11839–11844.

Meister, M., Lowe, G., and Berg, H. C. (1987). The proton flux through the bacterial flagellar motor. *Cell*,

49(5):643–650.

Monod, J., Wyman, J., and Changeux, J.-P. (1965). On the nature of allosteric transitions: a plausible model. *Journal of molecular biology*, 12(1):88–118.

Murphy, K. C. and Campellone, K. G. (2003). Lambda red-mediated recombinogenic engineering of enterohemorrhagic and enteropathogenic e. coli. *BMC Molecular Biology*, 4(1):11.

Nakamura, S. and Minamino, T. (2024). Structure and dynamics of the bacterial flagellar motor complex. *Biomolecules*, 14(12):1488.

Nirody, J. A., Nord, A. L., and Berry, R. M. (2019). Load-dependent adaptation near zero load in the bacterial flagellar motor. *Journal of the Royal Society Interface*, 16(159):20190300.

Niu, Y., Zhang, R., and Yuan, J. (2023). Flagellar motors of swimming bacteria contain an incomplete set of stator units to ensure robust motility. *Science Advances*, 9(44):eadi6724.

Nord, A. L., Gachon, E., Perez-Carrasco, R., Nirody, J. A., Barducci, A., Berry, R. M., and Pedaci, F. (2017). Catch bond drives stator mechanosensitivity in the bacterial flagellar motor. *Proceedings of the National Academy of Sciences*, 114(49):12952–12957.

O'Neill, J., Xie, M., Hijnen, M., and Roujeinikova, A. (2011). Role of the motb linker in the assembly and activation of the bacterial flagellar motor. *Biological Crystallography*, 67(12):1009–1016.

Ose, N. J., Butler, B. M., Kumar, A., Kazan, I. C., Sanderford, M., Kumar, S., and Ozkan, S. B. (2022). Dynamic coupling of residues within proteins as a mechanistic foundation of many enigmatic pathogenic missense variants. *PLoS Computational Biology*, 18(4):e1010006.

Ose, N. J., Campitelli, P., Modi, T., Kazan, I. C., Kumar, S., and Ozkan, S. B. (2024). Some mechanistic underpinnings of molecular adaptations of sars-cov-2 spike protein by integrating candidate adaptive polymorphisms with protein dynamics. *eLife*, 12:RP92063.

Prezhdo, O. V. and Pereverzev, Y. V. (2009). Theoretical aspects of the biological catch bond. *Accounts of Chemical Research*, 42(6):693–703.

Reboul, C. F., Andrews, D. A., Nahar, M. F., Buckle, A. M., and Roujeinikova, A. (2011). Crystallographic and molecular dynamics analysis of loop motions unmasking the peptidoglycan-binding site in stator protein motb of flagellar motor. *PLoS one*, 6(4):e18981.

Reid, S. W., Leake, M. C., Chandler, J. H., Lo, C.-J., Armitage, J. P., and Berry, R. M. (2006). The maximum number of torque-generating units in the flagellar motor of escherichia coli is at least 11. *Proceedings of the National Academy of Sciences*, 103(21):8066–8071.

Reynolds, K. A., McLaughlin, R. N., and Ranganathan, R. (2011). Hot spots for allosteric regulation on protein surfaces. *Cell*, 147(7):1564–1575.

Roujeinikova, A. (2008). Crystal structure of the cell wall anchor domain of motb, a stator component of the bacterial flagellar motor: implications for peptidoglycan recognition. *Proceedings of the National Academy of Sciences*, 105(30):10348–10353.

Santiveri, M., Roa-Eguiara, A., Kühne, C., Wadhwa, N., Hu, H., Berg, H. C., Erhardt, M., and Taylor, N. M.

(2020). Structure and function of stator units of the bacterial flagellar motor. *Cell*, 183(1):244–257.

Schindelin, J., Arganda-Carreras, I., Frise, E., Kaynig, V., Longair, M., Pietzsch, T., Preibisch, S., Rueden, C., Saalfeld, S., Schmid, B., et al. (2012). Fiji: an open-source platform for biological-image analysis. *Nature Methods*, 9(7):676–682.

Sowa, Y. and Berry, R. M. (2008). Bacterial flagellar motor. *Quarterly reviews of biophysics*, 41(2):103–132.

Stolz, B. and Berg, H. C. (1991). Evidence for interactions between mota and motb, torque-generating elements of the flagellar motor of escherichia coli. *Journal of Bacteriology*, 173(21):7033–7037.

Süel, G. M., Lockless, S. W., Wall, M. A., and Ranganathan, R. (2003). Evolutionarily conserved networks of residues mediate allosteric communication in proteins. *Nature structural biology*, 10(1):59–69.

Tinevez, J.-Y., Perry, N., Schindelin, J., Hoopes, G. M., Reynolds, G. D., Laplantine, E., Bednarek, S. Y., Shorte, S. L., and Eliceiri, K. W. (2017). Trackmate: An open and extensible platform for single-particle tracking. *Methods*, 115:80–90.

Tipping, M. J., Delalez, N. J., Lim, R., Berry, R. M., and Armitage, J. P. (2013). Load-dependent assembly of the bacterial flagellar motor. *MBio*, 4(4):10–1128.

Wadhwa, N. and Berg, H. C. (2022). Bacterial motility: machinery and mechanisms. *Nature Reviews Microbiology*, 20(3):161–173.

Wadhwa, N., Phillips, R., and Berg, H. C. (2019). Torque-dependent remodeling of the bacterial flagellar motor. *Proceedings of the National Academy of Sciences*, 116(24):11764–11769.

Wadhwa, N., Sassi, A., Berg, H. C., and Tu, Y. (2022). A multi-state dynamic process confers mechano-adaptation to a biological nanomachine. *Nature Communications*, 13(1):5327.

Wadhwa, N., Tu, Y., and Berg, H. C. (2021). Mechanosensitive remodeling of the bacterial flagellar motor is independent of direction of rotation. *Proceedings of the National Academy of Sciences*, 118(15):e2024608118.

Waterhouse, A., Bertoni, M., Bienert, S., Studer, G., Tauriello, G., Gumienny, R., Heer, F. T., de Beer, T. A. P., Rempfer, C., Bordoli, L., et al. (2018). Swiss-model: homology modelling of protein structures and complexes. *Nucleic Acids Research*, 46(W1):W296–W303.

Yuan, C., Chen, H., and Kihara, D. (2012). Effective inter-residue contact definitions for accurate protein fold recognition. *BMC Bioinformatics*, 13(1):292.

Zhu, S., Nishikino, T., Takekawa, N., Terashima, H., Kojima, S., Imada, K., Homma, M., and Liu, J. (2020). In situ structure of the vibrio polar flagellum reveals a distinct outer membrane complex and its specific interaction with the stator. *Journal of Bacteriology*, 202(4):10–1128.

Zhu, S., Takao, M., Li, N., Sakuma, M., Nishino, Y., Homma, M., Kojima, S., and Imada, K. (2014). Conformational change in the periplamic region of the flagellar stator coupled with the assembly around the rotor. *Proceedings of the National Academy of Sciences*, 111(37):13523–13528.